# Transport of finite-size particles in a turbulent Couette flow: The effect of particle shape and inertia

Guiquan Wang, Micheline Abbas, Zhaosheng Yu, Annaig Pedrono, Éric Climent

# Transport of finite-size particles in a turbulent Couette flow: The effect of particle shape and inertia

Guiquan Wang[a,b,c], Micheline Abbas[b,c,*], Zhaosheng Yu[d], Annaïg Pedrono[a], Eric Climent[a,c]

[a] Institut de Mécanique des Fluides de Toulouse, IMFT, Université de Toulouse, CNRS, Toulouse, France
[b] Laboratoire de Génie Chimique, Université de Toulouse, CNRS, Toulouse France
[c] FERMaT, Université de Toulouse,CNRS, INPT, INSA, UPS, Toulouse, France
[d] Department of Mechanics, Zhejiang University, Hangzhou 310027, China

A B S T R A C T

The transport of finite-size particles in a turbulent plane Couette flow has been studied by particle-resolved numerical simulations based on the Force Coupling Method. The influence of the deviation of particle shape from sphericity was addressed, using neutrally buoyant spheroids with aspect ratio ranging from 0.5 to 2. The particle transport was compared to the case where the inertia of spherical particles was varied by considering different particle densities (while keeping comparable Stokes number). This work has shown that close to the wall, the symmetry axis of oblate particles is almost parallel to the wall-normal direction and the major axis of prolate particles tends to align in the flow direction. Both types of particles have a kayaking type of rotation in the core region which yields homogeneous collisions. The spatial particle distribution is strongly correlated to coherent structures. However, strong deviations occur for the most inertial particles which accumulate in the near wall region. Successive stages of accumulation and release in the streaks are observed while the regeneration cycle of turbulence proceeds. The case of massless bubbles is characterized by a very strong correlation with the large scale vortices that span over the depth of the Couette gap. Even though the particles do not modify drastically the flow, they have some effect on the fluctuating energy, as suggested from the pdf. This effect is more clear for non-spherical particles compared to the spherical ones with various density ratios.

## 1. Introduction

Wall-bounded turbulent flows are populated by coherent flow structures that are largely responsible for enhancing heat and mass transfer (Robinson, 1991). Understanding the particle dynamics in these coherent flow structures is fundamental to understand and predict particle transport, entrainment and deposition in environmental systems or industrial processes. For example particles can form particle streaks near the wall where the vortical flow structures create suitable conditions for particle entrainment, and participate to particle deposition by conveying them from the core region to the wall region Kaftori et al. (1995).

The dynamics of wall-bounded turbulent flows is very rich, and the literature on this subject is abundant. We will focus in this introduction on some aspects related to our investigation. The key structures in wall-bounded turbulence are the spatially coherent, temporally evolving, large-scale streaks (wall-normal sweeps and ejections) and large-scale streamwise vortices. The turbulence is sustained through a sequence of linear (lift-up) and nonlinear (stretching and break-up) structure interactions, forming the so-called regeneration cycle (Hamilton et al., 1995; Jiménez and Pinelli, 1999). We are interested in the transport of finite-size particles in wall-bounded turbulent flows. By finite-size we mean that the particle diameter is comparable to or larger than the small scales of the flow.

Particles can modulate the flow regime if they sufficiently perturb the turbulence regeneration cycle. For example, in turbulent plane Couette flow, Wang et al. (2017) have shown in details that neutrally buoyant finite-size particles with moderate volume concentration hardly alter the coherent structures in plane Couette flow. This was in agreement with the observation of Brandt (2014). However particles with the same size and concentration enhance the turbulence in pressure driven flow, as observed experimentally by Matas et al. (2003) and confirmed later by many simulations (Yu et al., 2013; Loisel et al., 2013; Picano et al., 2015). In a more recent paper Wang et al. (2018), we have shown that turbulence enhancement in pressure-driven flow is due to the accumulation of

particles in ejection regions, leading to the modulation of the regeneration cycle stages (mainly the lift-up and the vortex stretching mechanisms). All these afore-mentioned studies were carried out with spherical particles.

If the particles are much smaller that the small eddies, they are considered as pointwise. Marchioli and Soldati (2002) have shown that the sweep and ejection events are effective in transferring these particles toward the wall and the core respectively. Pointwise inertial particles are known to accumulate in high strain rate regions while bubbles tend to move towards the core of vortical regions (Balachandar and Eaton, 2010).

As for non-spherical particles, they experience forces and torques that depend on particle orientation. In wall-bounded turbulent flow, their axis was shown to preferentially orient towards the fluid vorticity direction (Parsa et al., 2012; Voth and Soldati, 2017). The orientation dynamics of non-spherical particles depends on their aspect ratio $A_r$. Even in the simplest case, a pure shear laminar flow, the particle rotation rate depends on its aspect ratio (following Jeffery's orbit (Jeffery, 1922)). When coupled to translation, particle rotation leads to cross-streamline motion even in the absence of particle inertia. In addition, non-spherical particles experience torque from the local flow deformation, which possibly leads to preferential alignment. Because of the rich orientation dynamics, the flow statistics of two-phase flows might depend on the deviation of particles from sphericity, in a non-trivial way (Voth and Soldati, 2017; Einarsson et al., 2015b; Dabade et al., 2016).

Most studies performed with anisotropic particles considered particle transport by fluid, without accounting for the particle two-way coupling with the fluid flow structures. For non-spherical particles which size is small compared to the smallest turbulent flow structures, many properties of particle motion are similar between different turbulent flows since the fluid strain is dominated by small scales, which share universal properties. Zhang et al. (2001) have shown that prolate ellipsoidal inertial particles accumulate in the viscous sublayer of a dilute turbulent channel flow (in the ejection regions like spherical particles), and the aspect ratio influences their deposition rate. In the same flow configuration, Mortensen et al. (2008) and Marchioli et al. (2010) observed in addition that prolate particles exhibit preferential orientation in the streamwise direction, especially near the channel walls, the aspect ratio having a negligible effect on particle distribution in the flow. Recently, the particle rotation dynamics was a subject of interest in addition to particle orientation, both being dependent on the particle position: whether near the channel center (similar to homogeneous turbulence) or near the walls where the shear is strong. Zhao et al. (2015b) found that near the channel center, inertia-free spheroids were evenly distributed across the channel, the flattest disks ($A_r = 0.01$) mainly tumbling in the plane normal to the vorticity, whereas the longest ($A_r = 50$) rods spinning in the vorticity direction, as in homogeneous isotropic turbulence (Byron et al., 2015). Inertia was found to reduce the preferential spinning or tumbling leading to more isotropic rotation. Near the channel walls, Zhao et al. (2015b) observed that preferential orientation of spheroids in the streamwise direction is induced by the coherent flow structures. When the feedback forcing from the particles onto the flow is taken into account, turbulence intensity reduction was observed for a channel flow laden with prolate particles (Zhao et al., 2015a).

Studies on turbulent flows laden with finite-size non-spherical particles are scarce. Experiments of Parsa et al. (2012) in isotropic turbulence with nearly isolated neutrally buoyant rod-like particles with the axis being larger than the Kolmogorov scale confirmed the preferential alignment of the particle axis with the local fluid vorticity. Based on numerical simulations, they have shown that the particle rms rotation rate depends strongly on the aspect ratio with an abrupt reduction of 80% occurring for $A_r$ between 0.5 and 2. Do-Quang et al. (2014) showed that finite-size fibers in turbulent channel flow behave differently from pointwise particles. They accumulate in high-speed streaks, staying there due to collisions with the wall. In the channel core, they confirmed that fibers align with the mean flow vorticity direction. Closer to the wall the fibers tumble in the shear plane. Very close to the walls they become aligned in the flow direction. For oblate particles with $A_r = 1/3$ in turbulent channel flow, Niazi Ardekani et al. (2017) observed a drag reduction due to the absence of a near-wall particle layer which is otherwise found when particles are spherical. They mainly found that the symmetry axis of the oblate particles tend to be preferentially oriented normal to the channel walls in the near wall region. To the authors' knowledge, the transport of non-spherical particles in plane turbulent Couette flow configuration has not been considered so far.

We investigate in this paper a plane Couette flow, as it is a generic and simple configuration to point out interesting features of the complex dynamics of non-spherical (prolate and oblate) finite size particles. We focused particularly on particle rotation dynamics, orientation and transport within large-scale structures. We consider spheroidal particles of minor radius $r_p = L_y/40$ with aspect ratio from 0.5 to 2 (where $r_p$ and $L_y$ are the particle and Couette gap size respectively). Their behavior is compared to that of inertial spherical particles of radius $r_p = L_y/40$ with density ratio from 0 to 5. The Reynolds number is slightly above the onset of turbulence. The paper is organized as follows. In Section 2, the numerical method used for this study is detailed, with a special emphasis on its extension to simulate ellipsoidal shape particles. Validations tests are also presented. Section 3 provides the details of the suspension flow simulations carried out in turbulent Couette configuration, with the characteristic dimensionless numbers. The results are described in Section 4, where we mainly focus on the particle spatial distribution, their rotational dynamics, their residence time in flow rotational structures and correlation of particle distribution with main turbulent flow structures. The paper ends with a conclusion on the major findings.

## 2. Simulation method and validation

Direct numerical simulations of single-phase flows are performed by using the code JADIM for an incompressible Newtonian fluid (Calmet and Magnaudet, 1997). The unsteady 3-D Navier–Stokes equations discretized on a staggered grid are integrated in space using the finite volume method. All terms involved in the balance equations are written in a conservative form and are discretized using second order centered schemes in space. The solution is advanced in time by a second-order semi-implicit Runge–Kutta/Cranck Nicholson time stepping procedure and incompressibility is achieved by a pressure correction which is solution of a Poisson equation.

Numerical simulations of particle trajectories and suspension flow dynamics are based on multipole expansion of momentum source terms added to the Navier–Stokes equations (namely Force-Coupling Method as described in Maxey and Patel (2001), Lomholt and Maxey (2003) and Climent and Maxey (2009)). The comparison of FCM with other methods that belong to the class of Fictitious Domain methods can be found in a review by Maxey (2017) for particulate flows. FCM is based on a low-order, finite force multipole representation of the effect of the particles on the surrounding fluid flow. Although no-slip boundary condition is not strictly enforced at the particle surface, the flow field perfectly agrees with the exact solution within a typical distance of 10% of the radius away from the particle surface. Optimal results are obtained with FCM on a uniform grid with only 6 mesh grids along the diameter. Compared to other fictitious domain methods such as

direct forcing methods (immersed boundary method or immersed body method) we obtain the same level of accuracy but with less computing efforts. Flow dynamics is coupled to Lagrangian tracking of particles. The fluid is assumed to fill the entire simulation domain, including the particle volume. The fluid velocity and pressure fields are solutions of continuity Eq. (1) and momentum balance Eqs. (2) and (3).

$$\nabla \cdot \mathbf{u} = 0 \tag{1}$$

$$\rho \frac{D\mathbf{u}}{D\mathbf{t}} = -\nabla p + \mu \nabla^2 \mathbf{u} + \mathbf{f}(\mathbf{x}, t) \tag{2}$$

$$f_i(\mathbf{x}, t) = \sum_{n=1}^{N_p} F_i^n \triangle(\mathbf{x} - \mathbf{Y}^n(t)) + G_{ij}^n \frac{\partial}{\partial x_j} \triangle'(\mathbf{x} - \mathbf{Y}^n(t)) \tag{3}$$

The spatial force distribution $\mathbf{f}(\mathbf{x}, t)$ in the momentum balance Eq. (3) accounts for the presence of particles in the flow. It is written as a multipole expansion truncated after the second term. The first term of the expansion called the monopole represents the force $\mathbf{F}^n$ that the particle exerts on the fluid due to buoyancy, particle inertia and particle-to-particle contact forces (Eq. (23)). This monopole term balances the drag, added-mass, lift and history forces (Climent and Maxey, 2003).

$$\mathbf{F}^n = (m_p - m_f)\left(\mathbf{g} - \frac{d\mathbf{V}^n}{dt}\right) + \mathbf{F}_{ext}^n \tag{4}$$

The second term, called dipole, is based on a tensor $\mathbf{G}^n$ sum of two contributions: an anti-symmetric part $A_{ij}^n = \frac{1}{2}\epsilon_{ijk} T^n$ is related to the torque $\mathbf{T}^n$ applied on the particle, which is a combination of the external torque and inertial terms (Climent and Maxey, 2009), and a symmetric part which accounts for the rigidity of finite-size particle (Lomholt and Maxey, 2003).

$$\mathbf{T}^n = \mathbf{T}_{ext}^n - (I_p - I_f)\left(\frac{d\mathbf{\Omega}^n}{dt}\right) \tag{5}$$

where $I_p$ (resp. $I_f$) is the particle (resp. appropriate fluid) rotational inertia. The symmetric part $S_{ij}^n$ that accounts for the resistance of a rigid particle to local strain by ensuring zero average deformation inside the particle volume, Eq. (6).

$$E_{ij}^n(t) = \frac{1}{2}\int \left(\frac{\partial u_i}{\partial x_j} + \frac{\partial u_j}{\partial x_i}\right) \triangle'(\mathbf{x} - \mathbf{Y}^n(t)) d^3x = 0 \tag{6}$$

The particle finite-size is accounted for by spreading the momentum source terms around the particle center $\mathbf{Y}^n$ using a Gaussian spherical envelope. For an ellipsoidal particle having its principal axes aligned with the axes and its center located at the origin of the reference framework, the implicit equation of the surface is written in the form of Eq. (7).

$$\frac{x^2}{a^2} + \frac{y^2}{b^2} + \frac{z^2}{c^2} = 1 \tag{7}$$

where $a$, $b$ and $c$ are the lengths of its semi-axes.

In the frame of the Force Coupling Method, the Gaussian envelopes are adapted in order to take into account the particle shape. Therefore, the generalized Gaussian envelopes can be written for the monopole in Eq. (8) and dipole terms in Eq. (9), following Liu et al. (2009):

$$\triangle(\mathbf{x}) = (2\pi)^{-3/2}(\sigma_1\sigma_2\sigma_3)^{-1} \exp\left[-\frac{1}{2}\left(\frac{x^2}{{\sigma_1}^2} + \frac{y^2}{{\sigma_2}^2} + \frac{z^2}{{\sigma_3}^2}\right)\right] \tag{8}$$

$$\triangle'(\mathbf{x}) = (2\pi)^{-3/2}(\sigma_1'\sigma_2'\sigma_3')^{-1} \exp\left[-\frac{1}{2}\left(\frac{x^2}{\sigma_1'^2} + \frac{y^2}{\sigma_2'^2} + \frac{z^2}{\sigma_3'^2}\right)\right] \tag{9}$$

It was shown by the same authors that the widths of the Gaussian envelopes $\sigma_i$ (Eq. (10)) and $\sigma_i'$ (Eq. (11)) are related to the semi-axis $a$, $b$, $c$ similarly to a spherical shape.

$$\sigma_1 = a/\sqrt{\pi};\ \ \sigma_2 = b/\sqrt{\pi};\ \ \sigma_3 = c/\sqrt{\pi} \tag{10}$$

$$\sigma_1' = a/(6\sqrt{\pi})^{1/3};\ \ \sigma_2' = b/(6\sqrt{\pi})^{1/3};\ \ \sigma_3' = c/(6\sqrt{\pi})^{1/3} \tag{11}$$

In addition to the update of the particle positions, it is important to update the particle orientation in time. The general orientation of an ellipsoid is determined from the orthogonal unit vectors $\mathbf{p}_1$, $\mathbf{p}_2$ and $\mathbf{p}_3$ following the ellipsoid semi-axes. They rotate as a rigid body. Therefore, for a particle $n$, their evolution in time is obtained from the particle rotation velocity $\mathbf{\Omega}^n$ as:

$$\frac{d\mathbf{p}_i^n}{dt} = \mathbf{\Omega}^n \times \mathbf{p}_i^n \tag{12}$$

The transformation between the fixed coordinate axes of reference and the instantaneous semi-axes of an ellipsoid is specified by the orthogonal matrix $Q$:

$$Q = [\mathbf{p_1}^T, \mathbf{p_2}^T, \mathbf{p_3}^T] \tag{13}$$

The general form of the Gaussian envelop is then written as:

$$\triangle(\mathbf{x}) = (2\pi)^{-3/2}(\sigma_1\sigma_2\sigma_3)^{-1} \exp\left[-\frac{1}{2}\mathbf{x}^T Q^T \begin{pmatrix} \sigma_1^{-2} & 0 & 0 \\ 0 & \sigma_2^{-2} & 0 \\ 0 & 0 & \sigma_3^{-2} \end{pmatrix} Q\mathbf{x}\right] \tag{14}$$

$$\triangle'(\mathbf{x}) = (2\pi)^{-3/2}(\sigma_1'\sigma_2'\sigma_3')^{-1} \exp\left[-\frac{1}{2}\mathbf{x}^T Q^T \begin{pmatrix} \sigma_1'^{-2} & 0 & 0 \\ 0 & \sigma_2'^{-2} & 0 \\ 0 & 0 & \sigma_3'^{-2} \end{pmatrix} Q\mathbf{x}\right] \tag{15}$$

The separate temporal integration of the three particle unit vectors in Eq. (11) can lead to some inconsistency in the particle angular dynamics. Therefore, following Nikravesh et al. (1985) we replace the time integration of separate unit vectors $\mathbf{p}_i$ by the time integration of the quaternion $\mathbf{q}$ of a unit vector of an orientational axis of rotation. The derivative in time of the quaternion is related to the particle rigid motion as follows:

$$\frac{d\mathbf{q}^n}{dt} = \frac{1}{2}(\mathbf{A}^n)^T \times \mathbf{\Omega}^n \tag{16}$$

where $\mathbf{A}^T$ is the matrix detailed in Eq. (17).

$$\mathbf{A}^T = \begin{pmatrix} -q_1 & -q_2 & -q_3 \\ q_0 & q_3 & -q_2 \\ -q_3 & q_0 & q_1 \\ q_2 & -q_1 & q_0 \end{pmatrix} \tag{17}$$

The rotation matrix $\mathbf{R}$ (Eq. (18))

$$\mathbf{R} = 2\begin{pmatrix} q_0^2 + q_1^2 - 1/2 & q_1 - q_0 q_3 & q_1 q_3 + q_0 q_2 \\ q_1 q_2 + q_0 q_3 & q_0^2 + q_2^2 - 1/2 & q_2 q_3 - q_0 q_1 \\ q_1 q_3 - q_0 q_2 & q_2 q_3 + q_0 q_1 & q_0^2 + q_3^2 - 1/2 \end{pmatrix} \tag{18}$$

allows to obtain the projection of a vector $\mathbf{M}'$ from the particle coordinate system onto the Cartesian frame of reference $\mathbf{M}$ using:

$$\mathbf{M} = \mathbf{R}\mathbf{M}' \tag{19}$$

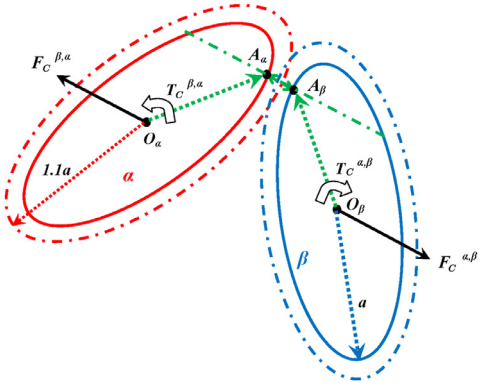


**Fig. 1.** Schematic representation of the repulsive force and torque at the center of a pair of ellipsoids if their surface is closer than a distance of $0.1(\| \mathbf{O}_\alpha\mathbf{A}_\alpha \| + \| \mathbf{O}_\beta\mathbf{A}_\beta \|)$.

With two perpendicular axes of the same length and a third one shorter (resp. longer), the ellipsoid is called oblate (resp. prolate) spheroid. Only spheroids will be considered in this work, within different flow configurations.

Furthermore, the particle translation and rotation velocities are obtained from a local weighted average of the volumetric fluid velocity (resp. rotational velocity) field over the region occupied by the particle (Eqs. (20) and (21)).

$$\mathbf{V}^n(t) = \int \mathbf{u}(\mathbf{x},t)\triangle(\mathbf{x}-\mathbf{Y}^n(t))d^3x \tag{20}$$

$$\mathbf{\Omega}^n(t) = \frac{1}{2}\int (\nabla\times\mathbf{u}(\mathbf{x},t))\triangle'(\mathbf{x}-\mathbf{Y}^n(t))d^3x \tag{21}$$

Particle trajectories are then obtained from numerical integration of the equation of motion as in Eq. (22).

$$\frac{d\mathbf{Y}^n}{dt} = \mathbf{V}^n \tag{22}$$

This modeling approach allows calculating the hydrodynamic interactions with a moderate computational cost. In order to capture correctly the dynamics of dilute suspension flow, four grid points per particle radius (for spherical particles) are usually required when the monopole force is not zero, and in the case where only dipole forcing is relevant, three grid points per particle radius are sufficient. For the simulation of ellipsoids, we ensure 3–4 grid points for within the semi-minor axis direction.

The repulsive model related to the distance between two particles (expressed as Eqs. (23) and (24)) is important to prevent the overlapping of non-spherical moving particles because it seriously influences the particle orientation and consequently their interaction with the flow. For a pair of ellipsoids $(\alpha)$ and $(\beta)$, the collision barrier is activated when the particles are very close. The minimal distance between the surfaces of two ellipsoids, or the surface of one ellipsoid and the wall, is calculated following Pope (2008) by successive approximations. The iterations stop when the difference between two successive iterations, $TOL = \|A_{\alpha,i}A_{\beta,i}\|_{min} - \| A_{\beta,i-1}A_{\alpha,i-1}\|_{min}$, is less than $0.001a$ ($a$ being the length of the major semi-axis). Note that for the aspect ratios used for this paper, $i = 8$–$10$ iterations are needed if we require $TOL \leq 0.001a$ and $i = 4$–$6$ iterations if $TOL \leq 0.01a$.

The contact force is added at the points of "contact" $A_\alpha$ and $A_\beta$ (which are the closest points between both particle surface) if their distance is less than $0.1(\| \mathbf{O}_\alpha\mathbf{A}_\alpha \| + \| \mathbf{O}_\beta\mathbf{A}_\beta \|)$. As shown in Fig. 1, the repulsive force at the contact point $A_\alpha$ is normal to the plane tangent to the surface at that point. This force is activated as soon as the two dashed ellipsoidal lines intersect with each other, the expanding factor being 1.1. Since the direction of the force does not necessarily pass through the ellipsoid center, the repulsive force $(\mathbf{F}_c^{\alpha\beta})$ is supplemented by a torque $(\mathbf{T}_c^{\alpha\beta})$, both of them being applied at the center of the ellipsoid $(O_\alpha)$. The force and torque applied on particle $(\alpha)$ are formulated in Eqs. (23) and (24).

$$\mathbf{F}_c^{\alpha\beta} = F_{ref}\left[1 - \frac{\| \mathbf{A}_\alpha\mathbf{A}_\beta \|^2}{(0.1\| \mathbf{O}_\alpha\mathbf{A}_\alpha \| + 0.1\| \mathbf{O}_\beta\mathbf{A}_\beta \|)^2}\right]\frac{\mathbf{A}_\alpha\mathbf{A}_\beta}{\| \mathbf{A}_\alpha\mathbf{A}_\beta \|} \tag{23}$$

$$\mathbf{T}_c^{\alpha\beta} = \mathbf{O}_\beta\mathbf{A}_\beta \times \mathbf{F}_c^{\alpha\beta} \tag{24}$$

However, if the particles actually overlap with each other, we impose a constant magnitude equal to $F_{ref}$. $F_{ref}$ is simply scaled with the Stokes drag force $F_d = 6\pi\mu\gamma a^2$ applied on a corresponding sphere based on characteristic particle relative velocity in shear flow $\gamma a$, where $a$ is the semi-major axis and $\gamma$ is the shear rate. In turbulent flow simulations through this paper, $F_{ref}$ was chosen such that the number of overlapping particles was found to be less than 1% of the total particle number. Simultaneously, the force $(\mathbf{F}_c^{\beta\alpha} = -\mathbf{F}_c^{\alpha\beta})$ and torque $(\mathbf{T}_c^{\beta\alpha} = \mathbf{O}_\alpha\mathbf{A}_\alpha \times \mathbf{F}_c^{\beta\alpha})$ are applied at $O_\beta$ of the other ellipsoid $(\beta)$. The forces and torques on both particles are added as external forces and torques to the FCM in Eqs. (4) and (5).

When particles are very close, lubrication due to fluid drainage within the gap between particle surfaces is not captured by FCM. This limits our present study to dilute or moderately concentrated suspensions. The repulsive model we used reproduces a soft contact between particles assuming no rebound. As shown in de Motta et al. (2013), when particles approach each other with a low impact Stokes numbers ($St < 10$), kinetic energy is damped by viscous dissipation in the fluid gap and no-rebound occurs. For all the simulations under investigation in this paper, the impact Stokes number is below the critical value for actual rebound.

Many tests were performed to validate the numerical approach, especially particle rotation under shear flow and the interaction of a pair of particles. Some of them will be discussed below.

### 2.1. Interaction of two spheroids in shear flow

This test is dedicated to validate the calculation of the Stresslet of an ellipsoid in a linear flow, and to verify if the collision barrier is suitable to recover the interaction of two ellipsoids. The reference case that we use for comparison is obtained with the Boundary Element method of Pozrikidis (2006) for Stokes flow.

We consider a pair of prolate spheroids in a linear flow. The initial orientation of the particles is $\varphi_0 = \pi/2$ and $\theta_0 = 0$ ($\mathbf{p}$ is oriented in the flow direction initially). Particle centers are separated in the streamwise direction by a distance $\Delta x$ before interaction. The two particle axes are rotating in the shear-gradient ($x$–$y$) plane during the interception. We select particle size $a = 0.1$, $b = c = 0.05$ and domain size $L_x \times L_y \times L_z = 1.5 \times 1 \times 0.5$ with a meshgrid of $95 \times 62 \times 32$ points. The particle Reynolds number in the FCM simulation is $Re_p = \gamma a^2/\nu = 0.1$, where $\gamma$ is the shear rate.

Fig. 2 shows a sequence of particle positions and orientations that compare very well with the result of Pozrikidis (2006) obtained with the same initial condition. The initial separation is $\Delta x = -10a$, $\Delta y = 1.5a$, $\Delta z = 0$. Snapshots of pair particle positions and orientations are selected at dimensionless instants $\gamma t = 0,\ 2.5,\ 5,\ 7.5,\ 10,\ 12.5,\ 15$.

Fig. 3 shows the evolution of the particle angular velocity $\Omega_z = d\theta/dt$ and shear Stresslet $G_{12}$ together with the corresponding evolution of an isolated particle. The results from FCM agree quantitatively well with Pozrikidis (2006) for Stokes flow. As stated by this author, the particle interception has only a weak effect on the effective viscosity and this effect is expected to become stronger when the particles interact under lubrication. The lubrication effect is not included neither in FCM nor in the spectral boundary-element method for Stokes flow.

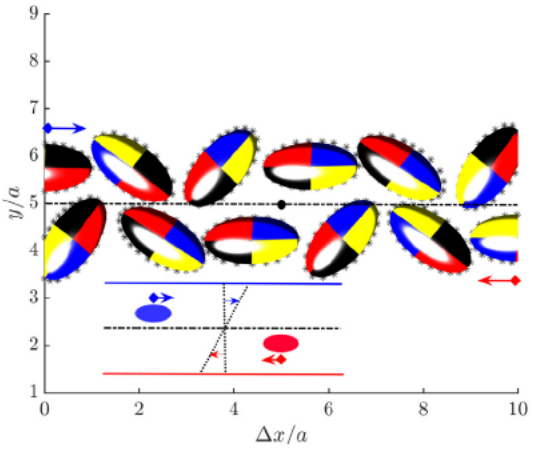


**Fig. 2.** Time sequence of two moving prolate spheroids with $Ar = 2$ within the shear-gradient plane for initial orientations $\varphi_0 = \pi/2$ and $\theta_0 = 0$. Asterisks show the ellipsoid surface from Pozrikidis (2006), four colors and solid line show FCM results. (For interpretation of the references to color in this figure legend, the reader is referred to the web version of this article.)

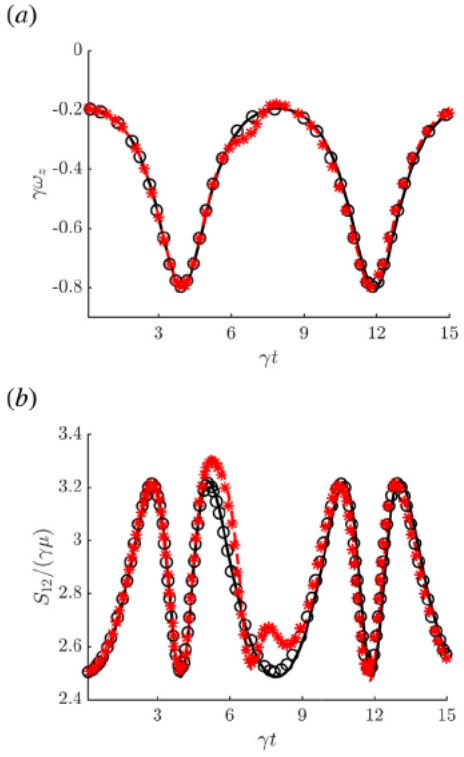


**Fig. 3.** Evolution of the rotation rate and the shearing component of the particle stress tensor during particle interception for $\varphi_0 = \pi/2$ and $\theta_0 = 0$. (*a*) the rate of rotation around the z axis; (*b*) particle stress tensor. —— FCM for an isolated spheroid; – – – FCM for pair of spheroids during interception; circle stands for an isolated spheroid and asterisks show the results for a pair of spheroids in Pozrikidis (2006).

As a complementary case study, the collision barrier force is tested on two particles approaching in a laminar Couette flow as shown in Fig. 4. For prolate spheroids ($a > b = c$), $F_{ref}$ is scaled by the Stokes drag force $F_d = 6\pi\mu\gamma a^2$. The prolate aspect ratio is $Ar = 2$ and the particle Reynolds number based on the largest particle dimension is $Re_p = \gamma a^2/\nu = 1$. When the repulsive force is activated (activation is related to separation distance less than $R_{ref}$), the two particle interaction is well recovered. The deviation, after collision, of the particles from the initial trajectories, depends on the value of $F_{ref}$.

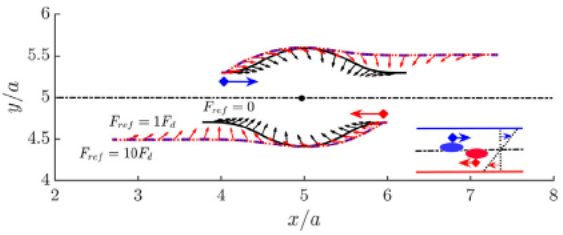


**Fig. 4.** Relative trajectories of a pair of neutrally buoyant prolate particles (blue and red) in laminar Couette flow with $Ar = 2$ and $Re_p = 1$. —— $F_{ref} = 0$; - - - - $F_{ref} = F_d$; – – – $F_{ref} = 10F_d$. Trajectories of $F_{ref} = F_d$ overlap with $F_{ref} = 10F_d$. The vector stands for the orientation of the symmetry axis for spheroidal particles during the process of interaction. (For interpretation of the references to color in this figure legend, the reader is referred to the web version of this article.)

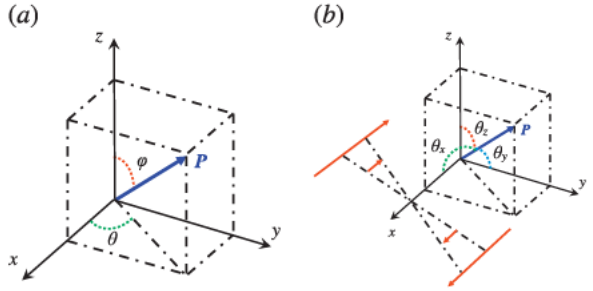


**Fig. 5.** Schematic diagram of a spheroid in shear flow: (*a*), $\phi$ is defined as the angle between **p** and the *z* direction, which is the vorticity direction in shear flow, and $\theta$ as the angle between the projection of **p** on the shear-gradient plane (*xy*) with the *x* direction; (*b*) $\theta_x$, $\theta_y$ and $\theta_z$ are the angles between **p** and the *x*, *y* and *z* direction, respectively.

### 2.2. Angular motion of an ellipsoid in shear flow

An ellipsoidal particle rotates with a non-uniform angular velocity in a shear flow, and the orbits depend on the particle aspect ratio, initial particle orientation, and eventually on the Reynolds number. At low Reynolds numbers, the particle rotates according to the well-known Jeffery's orbits, that are recalled here.

Consider a spheroid of aspect ratio $Ar$ in a linear flow $u = \gamma y$, where $\gamma$ is the shear rate in the shear-gradient plane ($x$–$y$). **p** is the unit vector along the symmetric axis of the spheroid. Fig. 5 show the angular definition of **p** in the frame of reference, using the spherical notation in (a) and cartesian notation in (b). Using the spherical notation for the angles, the projection of **p** on the Cartesian frame of reference is

$$\begin{aligned} p_x &= \sin\varphi\ \cos\theta \\ p_y &= \sin\varphi\ \sin\theta \\ p_z &= \cos\varphi \end{aligned} \tag{25}$$

Using the notation in (b),

$$\cos\theta_i = p_i, \quad i = x, y, z \tag{26}$$

with the relation $\cos^2\theta_x + \cos^2\theta_y + \cos^2\theta_z = 1$.

The theoretical prediction of rotation rate is expressed as the time derivative of $\theta$ and $\varphi$ in Eqs. (27) and (28).

$$\dot{\varphi} = -\left(\frac{Ar^2 - 1}{Ar^2 + 1}\right)\frac{\gamma}{4}\sin 2\varphi\ \sin 2\theta \tag{27}$$

and

$$\dot{\theta} = -\frac{\gamma}{Ar^2 + 1}(Ar^2\cos^2\theta + \sin^2\theta) \tag{28}$$

Simulations of spheroids with different aspect ratios and Reynolds numbers were carried out in linear flow, and some selected results on the particle rotational orbits are shown

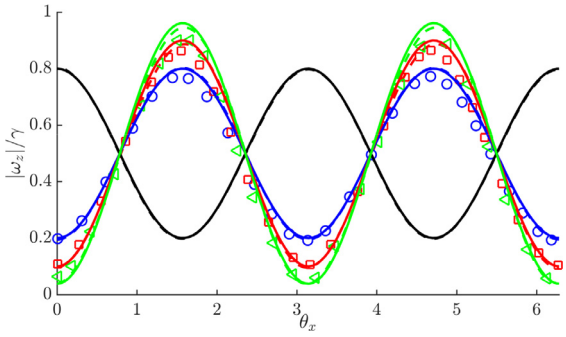


**Fig. 6.** Instantaneous angular velocity along the vorticity vector in a shear flow for spheroid (oblate $Ar = 0.5$ and prolate $Ar = 2 - 5$) in a suspension with volume fraction $\varphi = 0.058$. – – – FCM at $Re_p = 0.1$ compared with ——— Stokes solution of Jeffery. Colors distinguish four aspect ratios. Black: $Ar = 0.5$, blue: $Ar = 2$, red: $Ar = 3$ and green: $Ar = 5$. Symbols are results from Daghooghi and Borazjani (2015) at $Re_p = 0.01$ where ○: $Ar = 2$, □: $Ar = 3$ and ◁: $Ar = 5$. (For interpretation of the references to color in this figure legend, the reader is referred to the web version of this article.)

here. Furthermore, we performed numerical simulations using the direct-forcing fictitious domain (DF/FD) method from Yu and Shao (2007). The method is a non-Lagrange-multiplier version of the distributed-Lagrange-multiplier/fictitious-domain (DLM/FD) method proposed by Glowinski et al. (1999). Its accuracy and robustness are fully demonstrated in Yu and Shao (2007), in particular at low Reynolds numbers and for neutrally-buoyant particles. Both DF/FD and FCM are used in similar configurations, and the results are directly compared.

### 2.2.1. Effect of aspect ratio

The first test is realized at relatively low $Re_p$ (based on the semi-major axis and the shear rate) and aspect ratio $Ar$ that ranges between 0.5 and 5. $\mathbf{p}$ lays in the shear plane ($x$–$y$) and will stay there (since $\dot{\varphi} = 0$). Fig. 6 displays the angular velocity ($\Omega_z = d\theta/dt$) obtained by the FCM with $Re_p = 0.1$ compared to the Jeffery orbit (Stokes flow), and $Re_p = 0.01$ from the work of Daghooghi and Borazjani (2015) who used the curvilinear immersed-boundary method (CURVIB). The angular velocity resulting from FCM simulations are close to the theoretical solution over most of the period. For the prolate particle, the largest deviation takes place near the maximum velocity, when the prolate major axis is almost aligned with the shear direction. At the same angular orientation, the simulation from CURVIB shows even a smaller rotation rate at that orientation, especially when the symmetric axis $\mathbf{p}$ is perpendicular to the flow direction (e.g. $\theta$ is an odd multiples of $\pi/2$).

### 2.2.2. Effect of particle Reynolds number

The second test considers the effect of the Reynolds number on the ellipsoid rotation. In the case of a prolate spheroid with $Ar = 2$. The Reynolds number $Re_p$ ranges between 0.1 and 10. Fig. 7(a) shows that increasing the flow inertia tends to decrease the particle angular velocity, especially near the peaks, in agreement with the simulations of Daghooghi and Borazjani (2015).

Simulations using the FCM and DF/FD were run in the case of an oblate ($Ar = 0.5$) and prolate ($Ar = 2$) spheroids with the semi-minor axis length equal to 0.05 in a unit cubic computational domain at two Reynolds numbers ($Re_p = 1.0$ and $Re_p = 4.0$). The grid spatial resolution is of $64 \times 64 \times 64$ in FCM and $128 \times 128 \times 128$ in DF/FD. The rotational axis of the oblate spheroid is initially aligned with streamwise direction whereas it is aligned with the wall-normal direction for the prolate spheroid. The particle angular trajectory shown in Fig. 7(b), is calculated from both FCM and DF/FD methods. The results obtained from both methods agree very well

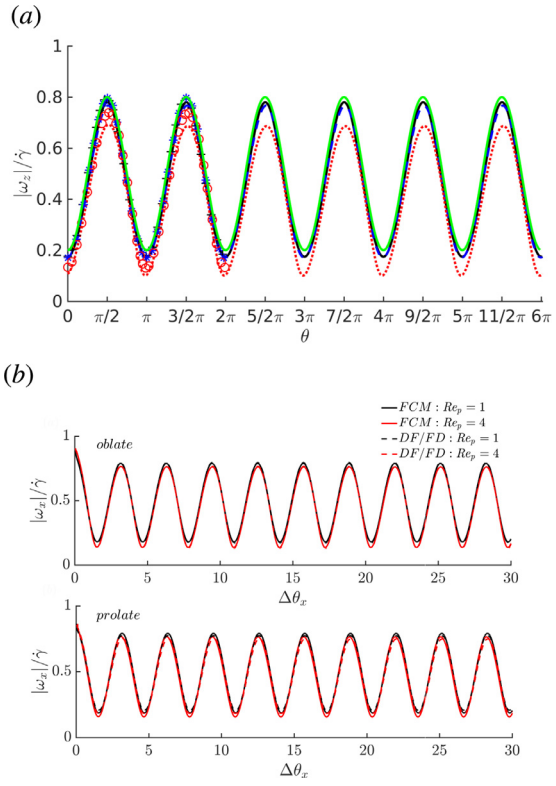


**Fig. 7.** Effect of the Reynolds number on the instantaneous angular velocity ($\omega_z = d\theta/dt$). ($a$): a prolate spheroid ($Ar = 2$) about the vorticity vector in a shear flow. The volume fraction is $\varphi = 0.058$. ——— Jeffery orbit. FCM: ——— $Re_p = 0.1$, – – – $Re_p = 1$ and ····· $Re_p = 10$. Symbols are results from Daghooghi and Borazjani (2015) where + : $Re_p = 0.1$, *: $Re_p = 1$ and ○: $Re_p = 10$; ($b$) is the comparison between FCM (line) and DF/FD (dash line): the top panel shows the symmetry axis of an oblate spheroid ($Ar = 0.5$) rotating about the vorticity vector at two Reynolds numbers, black is $Re_p = 1$ and red is $Re_p = 4$ ($Re_p$ is based on its semi-major axis). The bottom panel shows the symmetry axis of a prolate spheroid ($Ar = 2$) rotating about the vorticity vector. (For interpretation of the references to color in this figure legend, the reader is referred to the web version of this article.)

for the oblate spheroid whereas there is a small discrepancy for the prolate spheroid. In general, the FCM slightly overestimates the maximum prolate particle velocity (corresponding to the orientation along the shear direction), due to lower resolution near the particle endpoints.

### 2.2.3. Particle drift to stable orbit

The third test is related to the orientational dynamics of an ellipsoid which axis of symmetry is initially not in the shear plane neither parallel to the vorticity axis. Jeffery (1922) suggested that *the particles will tend to adopt that motion which, of all the motions possible under the approximated equations, corresponds to the least dissipation of energy.* Therefore the steady state orbit of a prolate spheroidal particle in a shear flow tends toward the spinning motion (particle major axis aligned with the vorticity direction), whereas the oblate spheroidal particles tend toward the tumbling motion (the axis of symmetry rotate in the shear plane). After 3 decades, Saffman (1956) showed that when the flow inertia is finite but small and the deviation from sphericity is small, the orbit at equilibrium is unchanged with respect to the inertialess regime, for both types of spheroids, a finding that was later confirmed by Subramanian and Koch (2006). This was revisited after recent simulations of (Qi and Luo, 2003; Yu et al., 2007; Huang et al., 2012; Rosén et al., 2014) who found the opposite: tumbling is the stable orbit for a prolate spheroid, whereas spinning is the stable one for oblate spheroid using a wide range of aspect ratio $1/3 < Ar < 3$ and particle Reynolds number $Re_p < 15$. This was

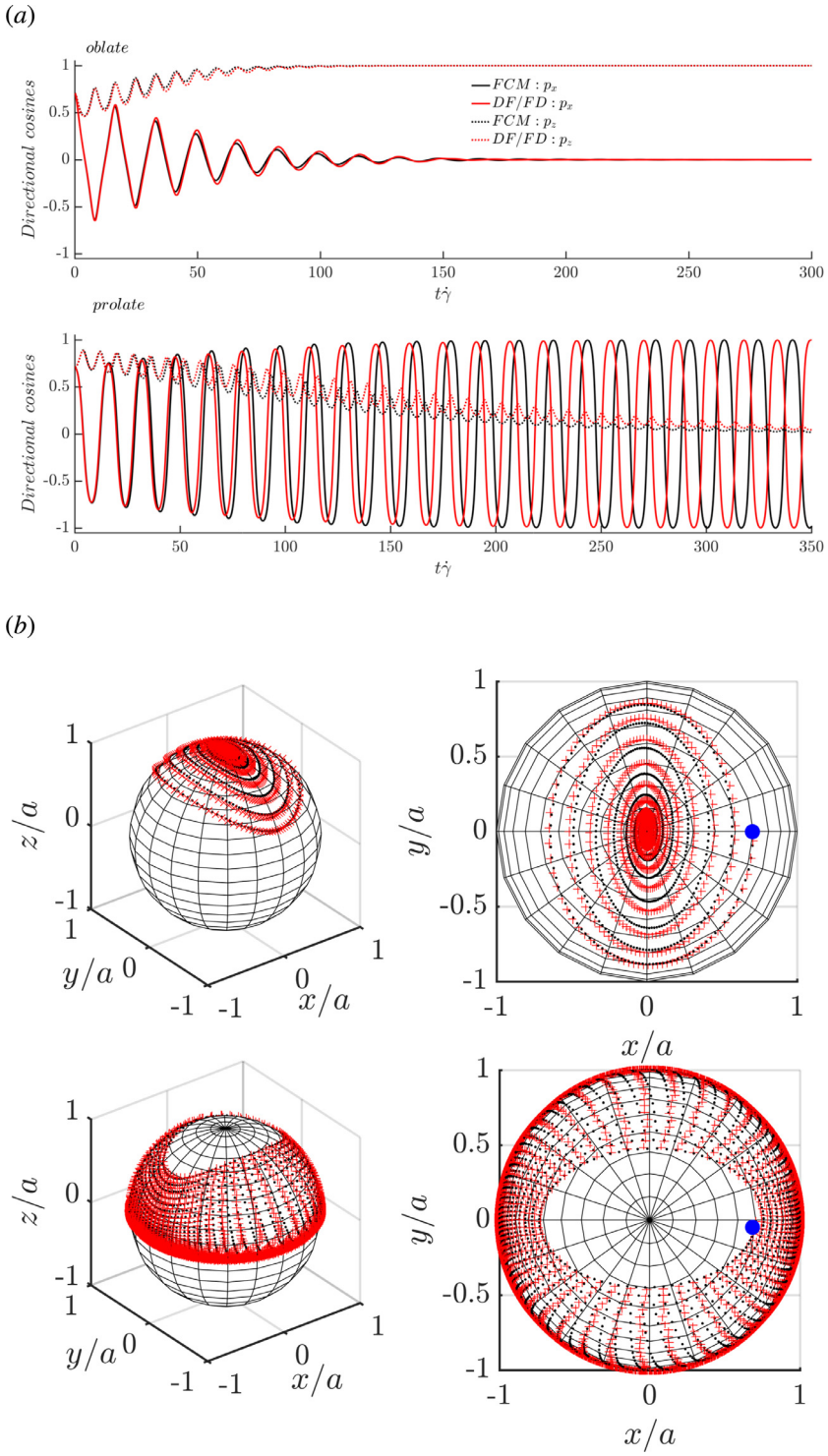


**Fig. 8.** Comparison of FCM and DF/FD: orientation vector **p** of a prolate and an oblate spheroid in simple shear flow at finite-size Reynolds number ($Re_p = 1.0$). (*a*) —— $\cos\theta_x(p_x)$, ----- $\cos\theta_z(p_z)$, red is for DF/FD and black is for FCM, the top panel corresponds to oblate spheroid and bottom panel for prolate particle; (*b*) projection of **p** on the unit sphere corresponding to (*a*) and the blue solid circle is the initial position of particle center, red cross is for DF/FD and black dot is for FCM, the top panel corresponds to oblate spheroid and bottom panel for prolate particle. (For interpretation of the references to color in this figure legend, the reader is referred to the web version of this article.)

later demonstrated theoretically by Einarsson et al. (2015a). Together with Dabade et al. (2016) they have shown that for thin oblates (close to disks) with aspect ratios $Ar < 1/7.3$, both tumbling and spinning are stable orbits, which makes the dilute suspension rheology not uniquely defined in theory.

In this test, neutrally buoyant prolate ($Ar = 2$) and oblate ($Ar = 0.5$) particles are considered and $Re_p = 1$ (based on the semi-major axis and the shear rate). The initial orientation is $\varphi_0 = \pi/4$ and $\theta_0 = \pi/2$. The domain size is set equal to $L_x = L_y = L_z = 5\max(a, b)$ for both simulations. The orientation orbits obtained with FCM and DF/FD are compared in Fig. 8. Directional cosines $p_x$ and $p_z$ of a

prolate and an oblate spheroid are plotted in Fig. 8(a). The convergence of a prolate (resp. oblate) particle toward stable tumbling (resp. log-rolling) orbits is a very slow process at low $Re_p = 0.125$. The convergence is faster at higher $Re_p$ (figure is not shown here). The angular trajectory of the oblate spheroid obtained by FCM is in good agreement with DF/FD. As for the prolate spheroid, in the first several orbits, FCM is in good agreement with DF/FD. Then the FCM tends to be slower than DF/FD to reach a stable state. We plot the orientation vector **p** on the unit sphere in Fig. 8(b). A nearly closed orbit is observed for the prolate spheroid after it drifts to a stable tumbling state whereas orientation vector **p** gets to a convergence point for the oblate spheroid after it drifts to a stable log-rolling state.

## 3. Suspension flow configuration

The turbulent plane Couette flow is generated by two walls moving in opposite directions with equal velocities, the dimensions of the domain being the same as the minimal flow unit Wang et al. (2017). Table 1 reports on all numerical parameters. The length and velocity are scaled by wall units $y^+ \equiv yu_\tau/\nu$, and $u^+ \equiv u/u_\tau$ where $u_\tau = \sqrt{\tau_w/\rho_f}$, $\tau_w$ being the wall shear stress. Although the Reynolds number in this paper is only slightly above the onset of turbulence (far from the regime of developed turbulence), we can give an estimate of the Kolmogorov scale $\eta/\delta_\nu \approx 1.5$ at the wall and $\eta/\delta_\nu = (\kappa y^+)^{0.25} \approx 2.0$ in the central region (Pope, 2000). All the cases of Table 1 fall in the range where the Force Coupling Method captures well the particle response to flow fluctuations (Wang et al., 2017). The results with neutrally buoyant spheroidal particles are compared with different particle-to-fluid density ratios. The size ratio between the Couette gap and the radius of smallest spherical particles $r_p$ used for this study is $L_y/r_p = 40$. The particle Reynolds number $Re_p \equiv \Gamma(V_r^{1/3}r_p)^2/\nu$ is based on local shear rate $\Gamma = |d\overline{u}/dy|$ and the effective radius evaluated from the particle volume $r_{eff} \equiv (V_r)^{1/3}r_p$. $V_r$ is the ratio of the spheroid volume to the reference sphere volume (see Table 1). The value of $F_{ref}$ in Eq. (23) has been set to $5F_d$ for all simulations. The Stokes number $St \equiv (2\rho_p/9\rho_f)Re_p$ takes into consideration the increase of inertia due to particle volume or to density ratio $\rho_r \equiv \rho_p/\rho_f$. The Stokes number defined here gives values close to the definition based on the relaxation time of non-spherical particles (summarized in Voth and Soldati (2017)). For example for $A_r = 2$ (resp $A_r = 0.5$), the Stokes number is 1.52 (resp 2.42) larger than the reference particle Stokes number when calculated from Voth and Soldati (2017) whereas the increase is 1.59 (resp 2.51) times in the present study.

## 4. Results on suspension flow in pCf

### 4.1. Particle spatial distribution

Fig. 9(a and b) show the spheroidal particle distribution and orientation in the ($y$–$z$) plane. The spheroids, like spheres as shown in Wang et al. (2017), tend to rather accumulate in the center of the vortices, whereas the strong ejection regions are quasi-free from particles. It is observed that at moderate inertia spatial particle distribution is not influenced by inertia when the particle shape is spheroidal (see bottom profiles in Fig. 9(c)). This observation holds for spherical particles with density ratio lower than 2. However, when the density ratio is equal to 5 (see concentration profiles in Fig. 9(c) for 10% concentration), the probability of finding particles accumulated close to Couette walls is significantly increased (peaks in the red dashed line). This is consistent with what has been observed for inertial pointwise spherical particles in turbulence (Balachandar and Eaton, 2010). However, this is different with inertial finite-size particles in pressure-driven turbulence (Fornari et al., 2016), who found the local volume fraction increases drastically at the centerline. Particle spatial distribution is hardly affected by the shape (at least to the aspect ratio we investigated), as it was already observed for pointwise inertial non-spherical particles in a channel flow (Mortensen et al., 2008; Marchioli et al., 2010). Indeed, for a lower aspect ratio ($Ar = 1/3$) and volume concentration lower than 10%, the concentration profile of oblate particles (Niazi Ardekani et al., 2017) is similar to spherical particles (Picano et al., 2015) in channel flow.

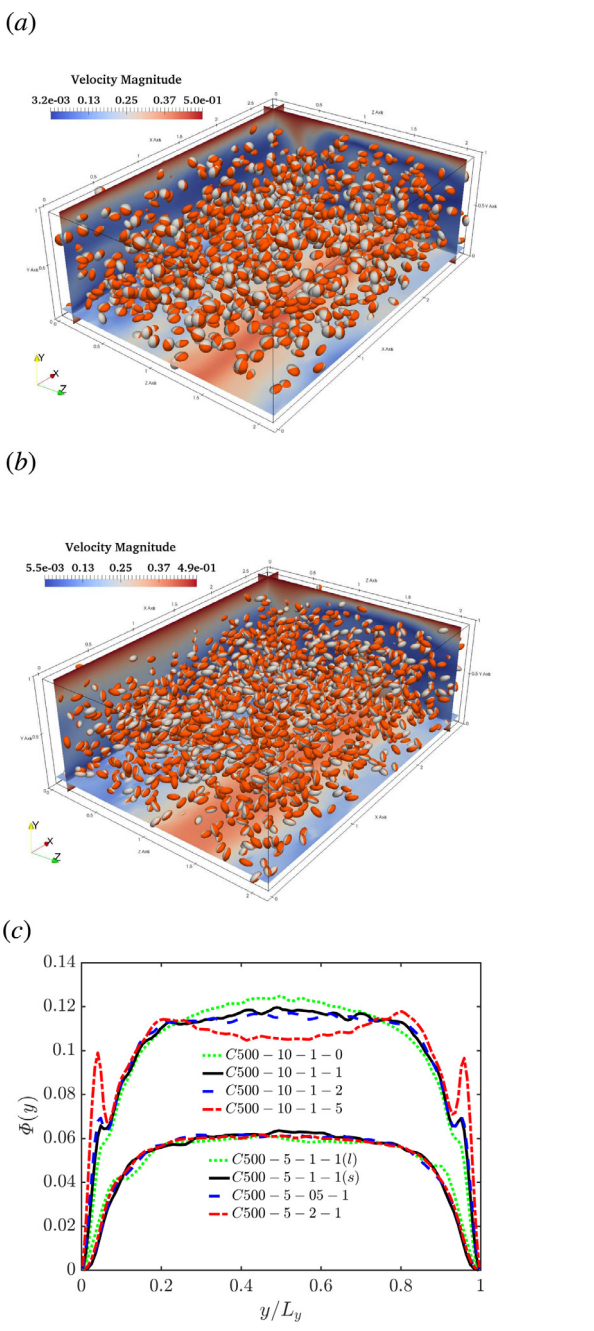


**Fig. 9.** ($a$) and ($b$) show the velocity magnitude and particle distribution with its orientation of C500-5-05-1 (oblate) and C500-5-2-1 (prolate particles), respectively. The figures are chosen when the large scale streaks are the strongest. The isocontours represent the instantaneous velocity magnitude in $y$–$z$ slice. ($c$) Particle concentration profiles for different particle shapes and density ratios. (For interpretation of the references to color in the text, the reader is referred to the web version of this article.)

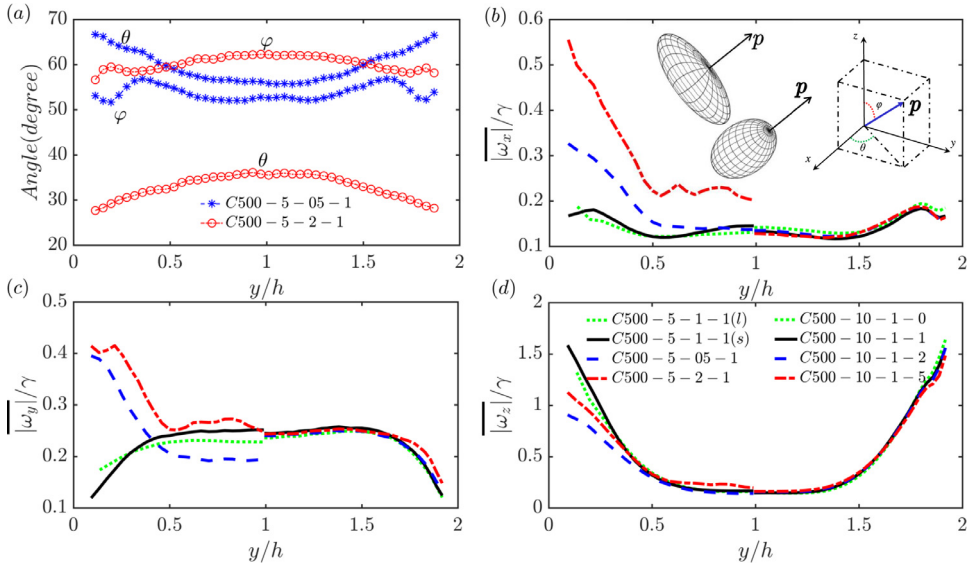


**Fig. 10.** (*a*) Wall-normal profiles of the particle orientation angles $\theta$ and $\varphi$ (projections of the **p** vector). The angle between the symmetry axis (**p** or $-$**p**) with the positive axis ($+x$ or $+z$) is used. $^*$ and $\circ$ stand for oblate and prolate particles respectively. (*b–d*): Profiles of the particle absolute angular velocity in streamwise ($\overline{|\omega_x|}$), wall-normal ($\overline{|\omega_y|}$) and spanwise ($\overline{|\omega_z|}$) directions normalized by the average shear rate $\gamma$. The shape effect is shown for $y/h<1$ and density ratio effect for $y/h>1$ on the same graph.

### *4.2. Particle rotation dynamics*

The rotation dynamics of spheroids in laminar plane Couette flow was already discussed in Section 2.2. As shown by Rosén et al. (2014), tumbling is the stable rotation orbit of a prolate spheroid, whereas spinning is the stable regime for oblate particles. Also in Section 2.2, we have shown that oblate and prolate spheroids both tend to migrate towards the core of a laminar pCf, no matter if the initial orientation of their symmetry axis is aligned with the vorticity (along $z$, the spanwise direction) or in the shear plane ($x$–$y$ plane).

Consider a spheroid with the unit vector **p** along the symmetry axis. The projection of **p** on the Cartesian frame of reference is given in Eq. (25), where the angles $\varphi$ and $\theta$ are defined in Fig. 10(b). The particle is mainly tumbling when $\varphi$ is close to 90° or spinning if $\varphi$ is close to 0. The angle $\theta$ indicates if the symmetry axis is rather oriented in the streamwise direction or along the shear direction.

In Fig. 10(a), we show the inclination angle of the symmetry axis instead of using cosine to avoid confusion in the averages since the cosine function is not linear. For oblate spheroids, both $\theta$ and $\varphi$ are relatively high, which means that oblate spheroids tend to move with the symmetry axis almost parallel to the wall-normal direction especially in the near wall region, indicating that oblate particles have more tumbling activity than spinning. This is similar to oblate spheroids with $A_r = 1/3$ in turbulent pressure-driven flow (Niazi Ardekani et al., 2017). However, prolate spheroids tend rather to align their major axis in the flow direction especially close to the wall and to tumble ($\varphi$ is large and $\theta$ is small in average). This is consistent with the observations in turbulent pressure-driven flow by Do-Quang et al. (2014).

The three components of particle absolute angular velocity are shown in Fig. 10(b–d). Near the walls, the particles rotate predominantly along the spanwise direction due to the mean shear. In the core region the dominant component is the rotation along the wall-normal direction ($\omega_y$). This is due to the gradient of the streamwise velocity in spanwise direction ($\partial u/\partial z$) which is formed by the gradient of streamwise velocity between low-speed (negative $u'$) and high-speed streaks (positive $u'$) in spanwise direction. For both types of spheroids, the particle rotation rate is decreased in the spanwise direction whereas it is increased in the other two directions, when compared to the spherical particle rotation rate. In the core region, the rotation rate in the three directions are non-zero, for both prolate and oblate spheroids. This indicates a kayaking type of motion similar to what has been observed for prolate spheroids in turbulent pressure-driven flow by Do-Quang et al. (2014). For spherical particles, the density ratio and concentration (from 5 to 10%) have both a negligible effect on the rotational rates in the three directions.

The kayaking type of rotation in the core region can yield homogeneous collisions. The three components of the particle collision forces are plotted in Fig. 11(a), where they were averaged in the homogeneous streamwise and spanwise directions. In the core region, the dominant collision force between spherical particles is in streamwise direction which is both due to particle collisions in ($x$–$z$) plane due to high- and low-speed streaks in that plane, and to the mean shear in the ($x$–$y$) plane (which is non-zero at the Couette center). This effect is enhanced by particle inertia as shown in Fig. 11(b). Near the Couette walls, the dominant component is in the wall-normal direction which is due to collisions occurring when particles are swept towards the walls. Fig. 11(c and d) show the collision forces scaled by $F_{ref}$. These forces give an indication on the momentum transfer by particle interactions. It is clear to see that at equal volume fraction, all the collision force component are much stronger when the particles are not spherical.

### *4.3. Probability density function of velocity fluctuations*

To characterize the particle transport by fluid flow structures, we focus on the buffer layer region, $0.15 < y/L_y < 0.5$ ($10 < y^+ < 40$), where the regeneration cycle governs the flow behavior (Jiménez, 2013). The probability density functions (PDF) of particle velocity fluctuations helps to describe if strong and weak fluctuations of particles are similar to that of the fluid. In Fig. 12(a and b), the PDFs of streamwise and wall-normal velocity fluctuations are shown, for simulations realized with different particle shapes and densities. Every panel compares the PDF of the particle velocity fluctuations with, on one hand, the fluid surrounding the particles in the two-phase simulations (which is not expected to

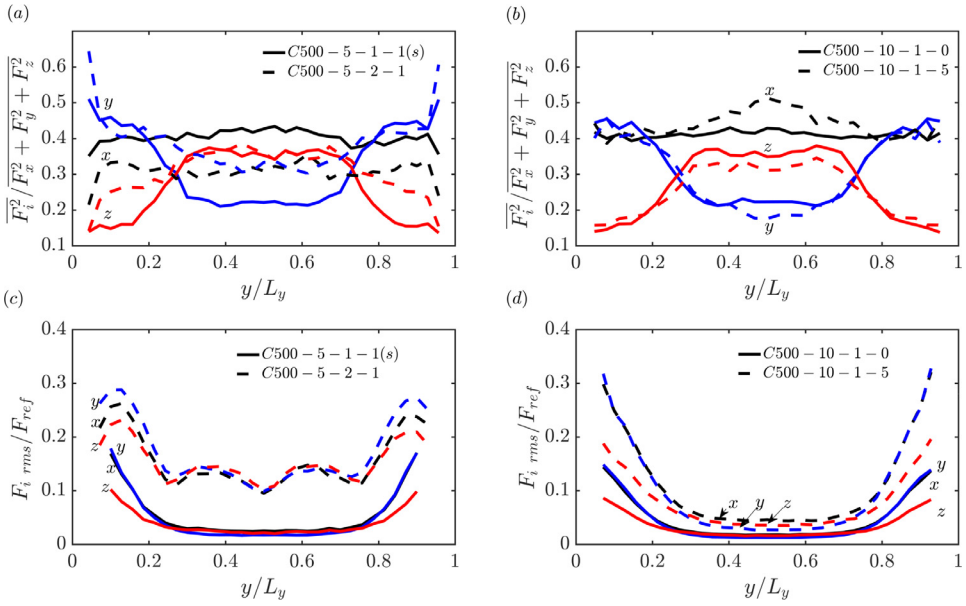


**Fig. 11.** Profiles of the repulsive force components ($F_i$) in directions $x$ black, $y$ blue and $z$ red. In ($a$) simulation results with spherical particles ——— C500-5-1-1(s) are compared to the simulations with prolate particles – – – C500-5-2-1. In ($b$) the effect of inertia is shown with cases ——— C500-10-1-0 and – – – C500-10-1-5. Corresponding to ($a$) and ($b$), ($c$) and ($d$) are the ratio between the repulsive force components with $F_d$. (For interpretation of the references to color in this figure legend, the reader is referred to the web version of this article.)

**Table 1**
Parameters of the numerical simulations. The Reynolds number of the singe-phase flow is $Re_b \equiv U_w h/\nu = 500$ where $U_w = 0.5$ is half of the relative wall velocity and $h = L_y/2$ is half of the Couette gap. $r_p = L_y/40$ is the radius of the reference sphere and $A_r$ is the aspect ratio between symmetry axis with rotation axis. The Stokes number is low near the Couette center (where the average shear rate is low) and maximum near the walls. Simulations start with a random initial seeding of particles which reach a steady statistical distribution after half period of the regeneration cycle. Then, statistics are formed over ∼500 time units ($h/U_w$).

Domain size: $L_x \times L_y \times L_z = 0.88\pi \times 1.0 \times 0.6\pi$

| Case | $\overline{\Phi}(\%)$ | $A_r$ | $\rho_r$ | $V_r$ | $L_y^+$ | $Re_\tau$ | $Re_p(max)$ | $St(max)$ | Line type |
|---|---|---|---|---|---|---|---|---|---|
| | | | | $N_x \times N_y \times N_z = 30 \times 86 \times 32$ | | | | | |
| Single-phase | – | – | – | – | 81 | 40.2 | – | – | + |
| Shape effect | | | | $N_x \times N_y \times N_z = 182 \times 66 \times 128$ | | | | | |
| C500-5-1-1(l) | 5 | 1 | 1 | 8 | 80.6 | 40.3 | 12.5 | 2.78 | ····· |
| | | | | $N_x \times N_y \times N_z = 280 \times 100 \times 256$ | | | | | |
| C500-5-1-1(s) | 5 | 1 | 1 | 1 | 80.6 | 40.3 | 3.75 | 0.83 | ——— |
| C500-5-05-1 | 5 | 0.5 | 1 | 4 | 80.1 | 40.0 | 6.9 | 1.53 | – – – |
| C500-5-2-1 | 5 | 2 | 1 | 2 | 81.4 | 40.2 | 3.5 | 0.78 | –·–·– |
| Inertia effect | | | | $N_x \times N_y \times N_z = 382 \times 134 \times 256$ | | | | | |
| C500-10-1-0 | 10 | 1 | $1.25\ 10^{-3}$ | 1 | 84.7 | 42.4 | 3.75 | $1.1\ 10^{-3}$ | ····· |
| C500-10-1-1 | 10 | 1 | 1 | 1 | 84.1 | 42.1 | 3.75 | 0.83 | ——— |
| C500-10-1-2 | 10 | 1 | 2 | 1 | 85.1 | 42.5 | 3.75 | 1.67 | – – – |
| C500-10-1-5 | 10 | 1 | 5 | 1 | 87.6 | 43.9 | 3.75 | 4.15 | –·–·– |

be significantly different from the particle velocity) and the single phase fluid flow fluctuations on the other hand.

The PDF of the wall-normal velocity fluctuations are almost Gaussian with zero mean and symmetric for all cases reported in Fig. 12. The PDF of the particle velocity fluctuations, and that of the surrounding fluid in the two-phase simulations are very similar to the single phase case, with a slight reduction of the peak at zero. The skewness of this distribution with the wall-normal velocity in the range $-0.1 < v'/U_w < 0.1$ is almost zero for single-phase flow (the skewness is equal to 0.034). This indicates that the intensities of wall-normal velocity fluctuations in inward and outward directions are statistically equal in the buffer layer of turbulent pCf.

The PDF of the streamwise velocity fluctuations are bimodal, with one velocity peak positive velocity and another one at negative velocity related to the ejection events. The intensity of negative $u'$ in low-speed streaks is stronger (but with a lower probability) than the positive $u'$ in high-speed streaks in the buffer layer, which is similar to what has been observed in turbulent pressure-driven flow (Kim et al., 1987). Particles increase slightly the probability of negative fluctuations, and shift the peak of positive velocity fluctuations toward smaller values.

### 4.4. Residence time of particles in LSVs

In homogeneous and isotropic turbulence, the time scale of the coherent motion of particles is comparable to the large-eddy turnover time (Bhatnagar et al., 2016). The most energetic structures of a turbulent plane Couette flow in the regime of weak turbulence, consist in pairs of contra-rotating Large Scale Vortices which size is comparable to the Couette gap and large scale streaks (Komminaho et al., 1996). The Large Scale Vortices (LSVs) carry significant fraction of turbulent kinetic energy (Pirozzoli et al., 2014).

In Wang et al. (2017), we found that the lightest particles tend to be trapped in the LSVs whereas heavy particles tend to move outward. The outward motion of particles by centrifugation from

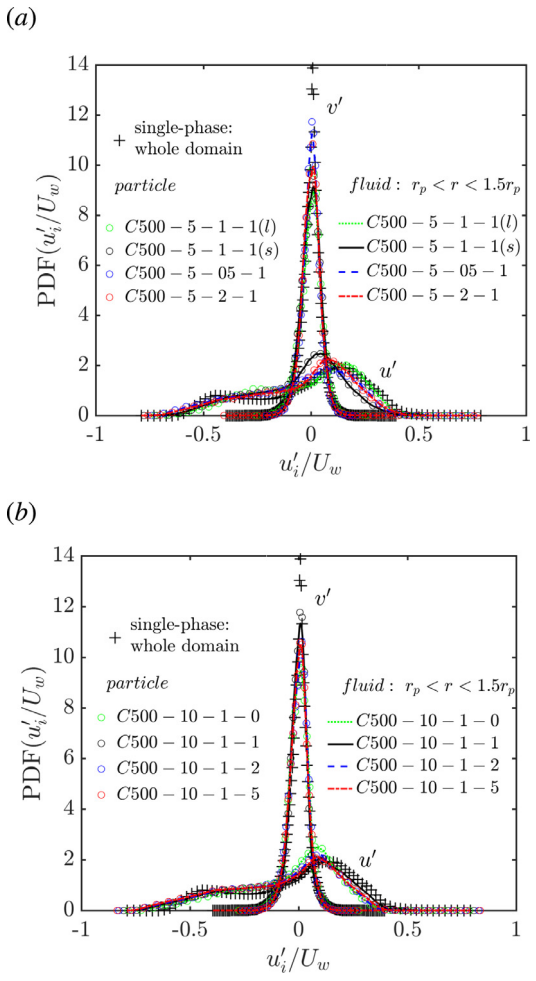


**Fig. 12.** Probability density functions of velocity fluctuations in the buffer layer ($10 < y^+ < 40$). Symbols represent the particle velocity (circles) and the single-phase flow fluctuations (crosses). In addition, the PDF of fluid fluctuation in a shell of thickness $0.5a$ around the particle surface is represented by lines which color legend according to Table 1). Both streamwise and wall-normal velocity components are shown, and the PDFs are averaged over ~400 time units. (*a*) shows the effect of particle shape and (*b*) the effect of particle-to-fluid density ratio. (For interpretation of the references to color in this figure legend, the reader is referred to the web version of this article.)

the flow coherent vortices influences particle dispersion, leading or not to preferential accumulation (Marshall, 1998). We have calculated the particle residence time in a vortex (mainly the large rolls) using the temporal evolution of the wall-normal position. In Fig. 13(a), the wall-normal position of oblate and prolate neutrally buoyant spheroids are plotted over time, in addition to the spherical particle trajectories. The spheroids behave qualitatively like neutrally-buoyant spherical particles, with a clear periodic oscillatory motion between both walls. Two distinct motions can be observed in the particle trajectories: a rotation in a single LSV for instance from *i* to *ii* and so on (dashed line of Fig. 13a), and a rotation of a particle in a LSV followed by its transfer to the other counter-rotating LSV from *iii* to *iv*.

In order to have a quantitative measure of the residence time in one vortex, we calculated Eq. (29) the temporal auto-correlation of the particle wall-normal position.

$$R_{yy}(\Delta t) = \frac{\overline{y'_p(t)\; y'_p(t+\Delta t)}}{y'^2_{p\ rms}} \tag{29}$$

where $y'_p$ is the fluctuation of the wall-normal particle position with respect to the average value, which was verified to be $h$ in the simulations (on average, the particles scan all the simulation domain equally).

Fig. 13(b and c) show the temporal auto-correlation functions. The auto-correlation function characterizes the particle large scale oscillatory motion. It becomes negative when the particle passes from one half of the Couette gap to the other, then almost zero when the particle leaves the large scale vortex. In Fig. 13(b and c) there are two sets of statistics. The particles that were trapped in a unique LSV were computed in one set, whereas the particles transferred from one LSV to the other were computed in another set.

The mean characteristic residence time of particles in a single LSV (set I) is $\sim 100U_w/h$ and $\sim 150U_w/h$ for particles that are transferred from one LSV to another LSV (set II). The smaller and lighter spherical particles have shorter periods in a single LSV whereas they have longer periods when they move from one LSV to the other. The residence time of particles in a single LSV approximately coincides with the period of the regeneration cycle observed by Hamilton et al. (1995), which indicates the strong relation between transport process of finite-size particles and the three sub-steps of the regeneration cycle in turbulent plane Couette flow.

### 4.5. Correlation of particle distribution with flow structures

The Reynolds shear stress contributions are classically divided into four quadrants: Q1(+*u*', +*v*'), Q2(−*u*', +*v*'), Q3(−*u*', −*v*'), Q4(+*u*', −*v*') where + means positive and means negative values of the velocity fluctuations. Beside large scale vortices, the x-independent streaks contribute the most to turbulent kinetic energy. The x-independent streaks predominantly consist in Q2$(-u', +v')$ and Q4$(+u', -v')$ regions (ejection and sweep respectively) which make the largest contributions to the Reynolds shear stress. They are offset from the interaction quadrants, Q1$(+u', +v')$ and Q3$(-u', -v')$, which are counter-gradient type motions (Wallace, 2016). The energy of this mode decreases during its breakdown to x-dependent streaks (wavy streaks). We show here that the accumulation of particles in the sweep and ejection regions is correlated, in time, to the evolution of the streaks and therefore to the regeneration cycle. For the temporal evolution of the streaky motion, it is represented by the modal analysis of the flow fluctuating energy. The Fourier decomposition of the energy over streamwise and spanwise directions, as introduced by Hamilton et al. (1995), is written as follows:

$$M(k_x = m\alpha, k_z = n\beta) \equiv \left\{ \int_{Y_1}^{Y_2} [\widehat{u'_i}\widehat{u'_i}(m\alpha, y, n\beta)]dy \right\}^{1/2} \tag{30}$$

where $Y_1$ and $Y_2$ stand for the integration bounds in wall-normal direction, ($\alpha$, $\beta$) are the fundamental wavenumbers in streamwise and spanwise directions defined as ($2\pi/L_x$, $2\pi/L_z$), and $m$ and $n$ are integers. Any turbulent structure can be represented by one mode ($m\alpha$, $n\beta$). For instance, the mode (0, $n\beta$) with $n \neq 0$ is an x-independent structure and the mode ($m\alpha$, $n\beta$) with $m \neq 0$ is the x-dependent structure (e.g. streaks confined in the streamwise direction). The temporal evolution of the x-independent streaks (mode (0, $\beta$)) is displayed in blue in Fig. 14(a–f), for suspension flows with different particle shapes and densities. Moreover, Fig 14 presents the temporal evolution of the percentage of particles contained within the streaky regions Q2 and Q4. The calculation was realized only in the buffer layers where the sweep and ejection events are strong, i.e. near the walls at $10 < y^+ < 40$. It can be noticed that more than half of the particles are contained within the sweep and ejection regions. The fluctuations in time of particle concentration in these regions are in-phase with the fluctuation of energy contained in the x-independent streaks. This is

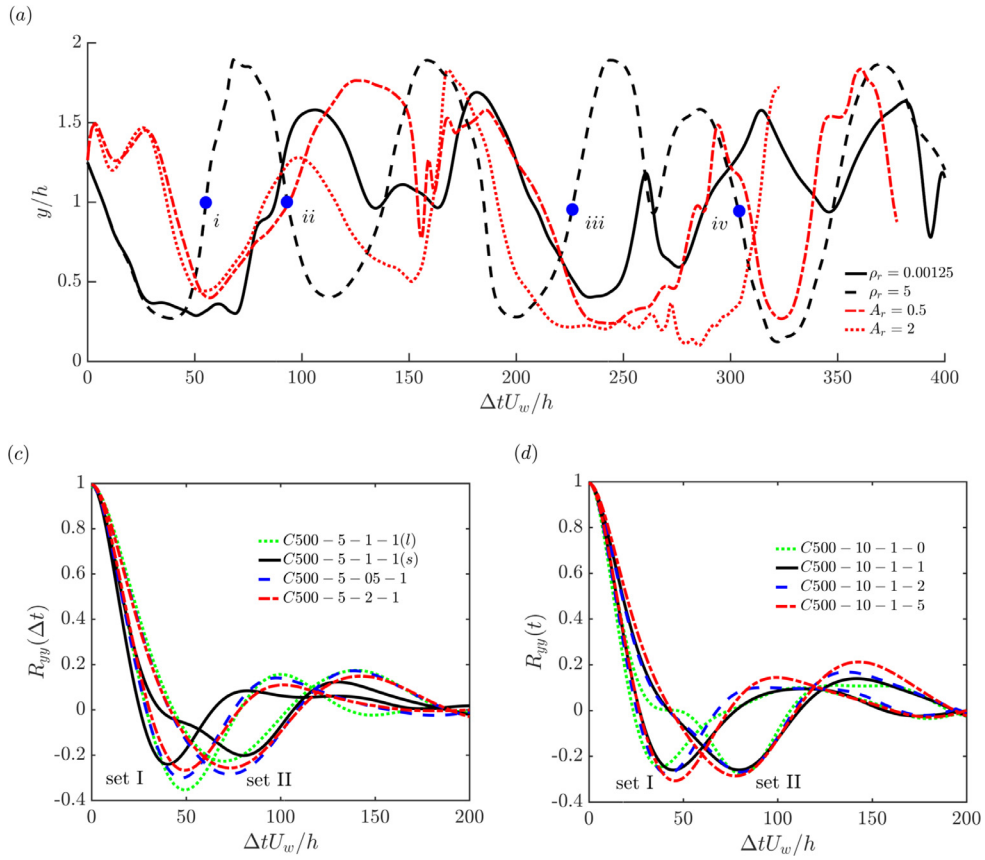


**Fig. 13.** (*a*) Temporal evolution of the wall-normal position of a particle in turbulent pCf at Reynolds number 500 for different particle shapes and densities: —— $\rho_r = 1.25\ 10^{-3}$; – – – $\rho_r = 5$ and -.-.- $A_r = 0.5$; ····· $A_r = 2$. (*b*) and (*c*) show the temporal auto-correlation functions of the wall-normal particle position fluctuation. The line style of (*b*) and (*c*) is shown in Table 1. Set I noted in these figures contains the statistics of particles trapped in one large scale vortex and set II contains particles transferred from one LSV to the other. The criteria used to attribute each particle to set I, set II or neither of the two sets, is based on $\Delta t_{min}$ at which the minimum of $R_{yy}$ corresponding to each particle occurs: if $\Delta t_{min} U_w/h < 60$, particle belongs to set I; if $60 < \Delta t_{\min} U_w/h < 100$, particle belongs to set II. Overall, 10–20 percents of the total number particles belong to each set.

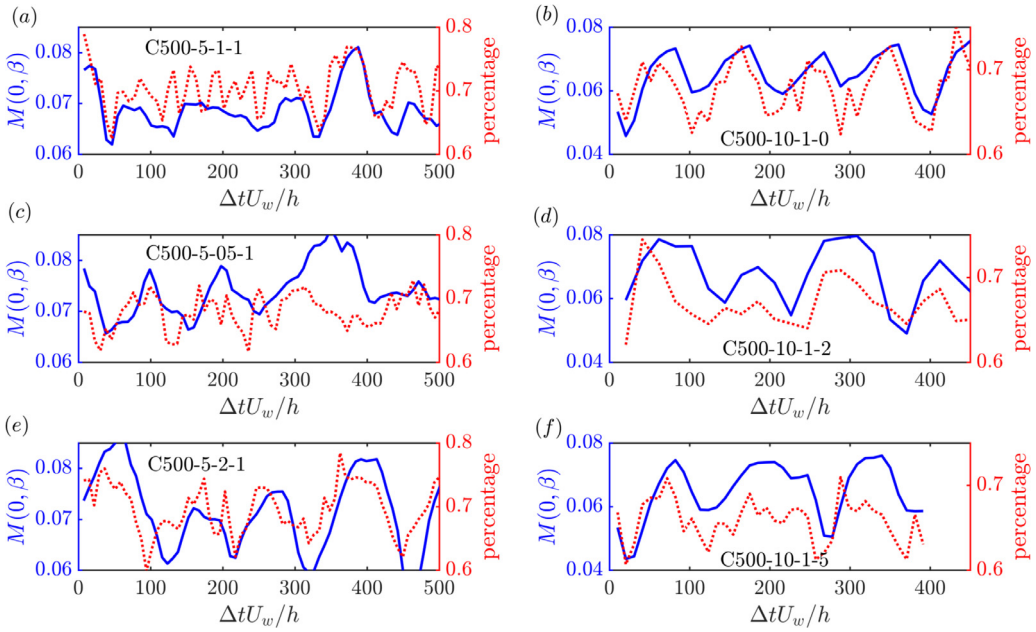


**Fig. 14.** Temporal evolution of mode $(0, n\beta)$ representing turbulent kinetic energy contained in the x-independent streaks (blue lines), and of the local particle percentage (ratio of particles in Q2 and Q4 to the total number of particles) in both ejection and sweep event regions (red dot lines). (*a, c, e*) show the particle shape effect with the cases from top to bottom: C500-5-1-1, C500-5-05-1 and C500-5-2-1. (*b, d, f*) show the effect of particle density, using from top to bottom: C500-10-1-0, C500-10-1-2 and C500-10-1-5. (For interpretation of the references to color in this figure legend, the reader is referred to the web version of this article.)

particularly evident at low Stokes numbers (C500-5-2-1 and C500-10-1-0). In the same context, we found that the percentage of particles contained in the Q1 and Q3 regions (not shown here) is correlated with the flow circulation, which is out-of-phase with the time evolution of x-independent streak energy.

## 5. Conclusion

The Force Coupling Method has been used for the simulation of spheroidal particles. The method has been validated for the specific cases of prolate and oblate ellipsoids. The configuration of a single spheroidal particle in shear flow has proven that FCM is suitable to handle the dynamics of finite-size particles. The agreement with theoretical predictions on the stable orbit is good and finite Reynolds effects have been compared to reference data simulation from literature. Then, results on a pair of spheroids interacting in a shear flow have been successfully compared to reference numerical data from boundary element method for Stokes flows.

We have investigated the spatial distribution and orientation statistics of finite-size particles in turbulent plane Couette flow for different inertia and shapes. When particles are neutrally buoyant, their overall dynamics is driven by the large scale turbulent structures of the fluid flow up to Stokes numbers ($St \approx 5$). However, we have observed that inertial spherical particles tend to accumulate more in the near wall region (for 10% volume concentration) than spheroids. This effect can be attributed to enhanced centrifugation of dense particles by longitudinal vortices and more diffusion of non-spherical particles due to their rotational dynamics and hydrodynamic interactions with the walls and among the suspension.

Because of the rich orientation dynamics, the flow statistics of two-phase flows might depend on the deviation of particles from sphericity, in a non-trivial way. Regarding rotational dynamics, many features of our study are confirming what has been observed in a turbulent channel flow. Oblate particles tend to move with the symmetry axis almost parallel to the wall-normal direction especially in the near wall region where they have more tumbling activity than spinning. However, prolate spheroids tend to align their major axis in the flow direction especially close to the wall. Near the walls, the particles rotate predominantly along the spanwise direction due to the mean shear. In the core region, the dominant component is the rotation along the wall normal direction with a kayaking type of motion yielding to direct interactions among spheroids enhancing the spreading of the suspension.

The typical residence time of a single particle in a large scale vortex is equal to the characteristic time scale of the regeneration cycle of turbulence. At equivalent volume fraction, the particle distribution of spheroids in the flow is not significantly altered by their shape (prolate or oblate). Particles are on average more present inside the large scale streamwise vortices, compared to the x-independent streaks. However, instantaneous particle spatial distribution depends on the successive steps of turbulence regeneration cycle. The ejection regions are seeded by more particles during streak formation (when the x-independent structures are energetic) and they release particles during streak breakdown (when the energy of x-independent structures is reduced). During streak formation (resp. breakdown), the flow circulation decreases (resp. increases), and the Q1 region mainly located inside large scale vortices loses (resp. gains) particles, migrating toward (resp. coming from) large scale streaks.

The next steps towards the numerical modeling of real suspensions would be to include the effects of polydispersity in size and shapes for given material properties of particles and then evaluate the overall response of the suspension in order to propose effective rheological properties for engineering applications.


## Acknowledgments

This work was granted access to the HPC resources of CALMIP under the allocation 2016 and 2017-P1002. G. Wang would like to thank Dr. Wenchao Yu for helpful discussions on the data analysis. Z. Yu acknowledges the support from the National Natural Science Foundation of China (Grant No. 91752117).


## References


Balachandar, S., Eaton, J.K., 2010. Turbulent dispersed multiphase flow. Annu. Rev. Fluid. Mech. 42, 111–133.

Bhatnagar, A., Gupta, A., Mitra, D., Pandit, R., Perlekar, P., 2016. How long do particles spend in vortical regions in turbulent flows? Phys. Rev. E 94 (5), 053119.

Brandt, L., 2014. The lift-up effect: the linear mechanism behind transition and turbulence in shear flows. Eur. J. Mech. B. Fluids 47, 80–96.

Byron, M., Einarsson, J., Gustavsson, K., Voth, G., Mehlig, B., Variano, E., 2015. Shape-dependence of particle rotation in isotropic turbulence. Phys. Fluids 27 (3), 035101.

Calmet, I., Magnaudet, J., 1997. Large-eddy simulation of high-schmidt number mass transfer in a turbulent channel flow. Phys. Fluids 9 (2), 438–455.

Climent, E., Maxey, M., 2003. Numerical simulations of random suspensions at finite reynolds numbers. Int. J. Multiphase Flow 29 (4), 579–601.

Climent, E., Maxey, M.R., 2009. The force coupling method: a flexible approach for the simulation of particulate flows. In: Feuillebois, F., Sellier., A. (Eds.), Inserted in 'Theoretical Methods for Micro Scale Viscous Flows'. Ressign Press.

Dabade, V., Marath, N.K., Subramanian, G., 2016. The effect of inertia on the orientation dynamics of anisotropic particles in simple shear flow. J. Fluid Mech. 791, 631–703. 3

Daghooghi, M., Borazjani, I., 2015. The influence of inertia on the rheology of a periodic suspension of neutrally buoyant rigid ellipsoids. J. Fluid Mech. 781, 506–549.

de Motta, J.B., Breugem, W.P., Gazanion, B., Estivalezes, J.L., Vincent, S., Climent, E., 2013. Numerical modelling of finite-size particle collisions in a viscous fluid. Phys. Fluids 25 (8), 083302.

Do-Quang, M., Amberg, G., Brethouwer, G., Johansson, A.V., 2014. Simulation of finite-size fibers in turbulent channel flows. Phys. Rev. E 89 (1), 013006.

Einarsson, J., Candelier, F., Lundell, F., Angilella, J., Mehlig, B., 2015a. Effect of weak fluid inertia upon Jeffery orbits. Phys. Rev. E 91 (4), 041002.

Einarsson, J., Candelier, F., Lundell, F., Angilella, J., Mehlig, B., 2015b. Rotation of a spheroid in a simple shear at small Reynolds number. Phys. Fluids 27 (6), 063301.

Fornari, W., Formenti, A., Picano, F., Brandt, L., 2016. The effect of particle density in turbulent channel flow laden with finite size particles in semi-dilute conditions. Phys. Fluids 27 (8), 083301.

Glowinski, R., Pan, T.W., Hesla, T.I., Joseph, D.D., 1999. A distributed lagrange multiplier/fictitious domain method for particulate flows. Int. J. Multiphase Flow 25 (5), 755–794.

Hamilton, J.M., Kim, J., Waleffe, F., 1995. Regeneration mechanisms of near-wall turbulence structures. J. Fluid Mech. 287, 317–348.

Huang, H., Yang, X., Krafczyk, M., Lu, X.Y., 2012. Rotation of spheroidal particles in Couette flows. J. Fluid Mech. 692, 369–394.

Jeffery, G.B., 1922. The motion of ellipsoidal particles immersed in a viscous fluid. In: Proceedings of the Royal Society of London A: Mathematical, Physical and Engineering Sciences. 102. The Royal Society, pp. 161–179.

Jiménez, J., 2013. Near-wall turbulence. Phys. Fluids 25 (10), 101302.

Jiménez, J., Pinelli, A., 1999. The autonomous cycle of near-wall turbulence. J. Fluid Mech. 389, 335–359.

Kaftori, D., Hetsroni, G., Banerjee, S., 1995. Particle behavior in the turbulent boundary layer.i. motion, deposition, and entrainment. Phys. Fluids 7 (5), 1095–1106.

Kim, J., Moin, P., Moser, R., 1987. Turbulence statistics in fully developed channel flow at low Reynolds number. J. Fluid Mech. 177, 133–166.

Komminaho, J., Lundbladh, A., Johansson, A.V., 1996. Very large structures in plane turbulent Couette flow. J. Fluid Mech. 320, 259–285.

Liu, D., Keaveny, E.E., Maxey, M.R., Karniadakis, G.E., 2009. Force-coupling method for flows with ellipsoidal particles. J. Comput. Phys. 228 (10), 3559–3581.

Loisel, V., Abbas, M., Masbernat, O., Climent, E., 2013. The effect of neutrally buoyant finite-size particles on channel flows in the laminar-turbulent transition regime. Phys. Fluids 25 (12), 123304.

Lomholt, S., Maxey, M.R., 2003. Force-coupling method for particulate two-phase flow: Stokes flow. J. Comput. Phys. 184 (2), 381–405.

Marchioli, C., Fantoni, M., Soldati, A., 2010. Orientation, distribution, and deposition of elongated, inertial fibers in turbulent channel flow. Phys. Fluids 22 (3), 033301.

Marchioli, C., Soldati, A., 2002. Mechanisms for particle transfer and segregation in a turbulent boundary layer. J. Fluid Mech. 468, 283–315.

Marshall, J., 1998. A model of heavy particle dispersion by organized vortex structures wrapped around a columnar vortex core. Phys. Fluids 10 (12), 3236–3238.

Matas, J.P., Morris, J.F., Guazzelli, E., 2003. Transition to turbulence in particulate pipe flow. Phys. Rev. Lett. 90, 014501.

Maxey, M., 2017. Simulation methods for particulate flows and concentrated suspensions. Annu. Rev. Fluid. Mech. 49, 171–193.

Maxey, M., Patel, B., 2001. Localized force representations for particles sedimenting in stokes flow. Int. J. Multiphase Flow 27 (9), 1603–1626.

Mortensen, P.H., Andersson, H.I., Gillissen, J.J., Boersma, B.J., 2008. On the orientation of ellipsoidal particles in a turbulent shear flow. Int. J. Multiphase Flow 34 (7), 678–683.
Niazi Ardekani, M., Costa, P., Breugem, W.P., Picano, F., Brandt, L., 2017. Drag reduction in turbulent channel flow laden with finite-size oblate spheroids. J. Fluid Mech. 816, 43–70.
Nikravesh, P.E., Wehage, R., Kwon, O., 1985. Euler parameters in computational kinematics and dynamics. J. Mech. Transm. Autom. Des. 107 (3), 358–365.
Parsa, S., Calzavarini, E., Toschi, F., Voth, G.A., 2012. Rotation rate of rods in turbulent fluid flow. Phys. Rev. Lett. 109 (13), 134501.
Picano, F., Breugem, W.P., Brandt, L., 2015. Turbulent channel flow of dense suspensions of neutrally buoyant spheres. J. Fluid Mech. 764, 463–487.
Pirozzoli, S., Bernardini, M., Orlandi, P., 2014. Turbulence statistics in couette flow at high reynolds number. J. Fluid Mech. 758, 327–343.
Pope, S.B., 2000. Turbulent flows. Cambridge university press.
Pope, S.B., 2008. Algorithms for Ellipsoids. Report No. FDA. Cornell University. 08–01
Pozrikidis, C., 2006. Interception of two spheroidal particles in shear flow. J. Non-Newtonian Fluid Mech. 136 (1), 50–63.
Qi, D., Luo, L.S., 2003. Rotational and orientational behaviour of three-dimensional spheroidal particles in couette flows. J. Fluid Mech. 477, 201–213.
Robinson, S.K., 1991. Coherent motions in the turbulent boundary layer. Annu. Rev. Fluid. Mech. 23 (1), 601–639.
Rosén, T., Lundell, F., Aidun, C., 2014. Effect of fluid inertia on the dynamics and scaling of neutrally buoyant particles in shear flow. J. Fluid Mech. 738, 563–590.
Saffman, P., 1956. On the motion of small spheroidal particles in a viscous liquid. J. Fluid Mech. 1 (05), 540–553.
Subramanian, G., Koch, D., 2006. Inertial effects on the orientation of nearly spherical particles in simple shear flow. J. Fluid Mech. 557, 257–296.
Voth, G.A., Soldati, A., 2017. Anisotropic particles in turbulence. Annu. Rev. Fluid. Mech. 49, 249–276.
Wallace, J.M., 2016. Quadrant analysis in turbulence research: history and evolution. Annu. Rev. Fluid. Mech. 48, 131–158.
Wang G., Abbas M. and Climent E., Modulation of the regeneration cycle by neutrally buoyant finite-size particles, J. Fluid Mech. Accepted. Available online on arXiv:1806.02862.
Wang, G., Abbas, M., Climent, E., 2017. Modulation of large-scale structures by neutrally buoyant and inertial finite-size particles in turbulent couette flow. Phys. Rev. Fluids 2 (8), 084302.
Yu, Z., Phan-Thien, N., Tanner, R.I., 2007. Rotation of a spheroid in a Couette flow at moderate Reynolds numbers. Phys. Rev. E 76 (2), 026310.
Yu, Z., Shao, X., 2007. A direct-forcing fictitious domain method for particulate flows. J. Comput. Phys. 227 (1), 292–314.
Yu, Z., Wu, T., Shao, X., Lin, J., 2013. Numerical studies of the effects of large neutrally buoyant particles on the flow instability and transition to turbulence in pipe flow. Phys. Fluids 25 (4), 043305.
Zhang, H., Ahmadi, G., Fan, F.G., McLaughlin, J.B., 2001. Ellipsoidal particles transport and deposition in turbulent channel flows. Int. J. Multiphase Flow 27 (6), 971–1009.
Zhao, F., George, W., Van Wachem, B., 2015a. Four-way coupled simulations of small particles in turbulent channel flow: the effects of particle shape and stokes number. Phys. Fluids 27 (8), 083301.
Zhao, L., Challabotla, N.R., Andersson, H.I., Variano, E.A., 2015b. Rotation of nonspherical particles in turbulent channel flow. Phys. Rev. Lett. 115 (24), 244501.